CHAPTER III

EXPERIMENTAL DETAILS

The experimental details of sample fabrication by droplet molecular beam epitaxy in this work are described in this chapter. The calibration of growth was done by *in situ* reflection high-energy electron diffraction observation, scanning electron microscopy and high resolution x-ray diffraction measurement. The sample morphologies, cross-sections and their optical properties were characterized by atomic force microscopy, transmission electron microscopy and photoluminescence spectroscopy.

3.1 Molecular Beam Epitaxy

molecular beam epitaxy (MBE) is a versatile technique for growing thin epitaxial structures that made of insulators, oxides, semiconductors or metals. Many MBE systems of III-V compound semiconductors have been developed, for example, gas-source MBE (GS-MBE) using hydrides as group-V materials such as arsine (AsH_3) or phosphine (PH_3), metal-organic MBE (MO-MBE) using metalorganic compounds as group-III materials such as triethylgallium (TEGa) and trimethylindium (TMIn), and solid-source MBE (SS-MBE) using solid-source materials such as indium (In) and Arsenic (As) to produce group-III and group-V molecular beam sources. Although each system has the different type of sources, they share the same growth principle. MBE process is based on the interaction of thermal-energy atomic or molecular beams of the constituent elements and a heated crystalline surface under ultra-high vacuum (UHV) conditions. The UHV environment is required in order to reduce the background pressure of contaminants, therefore MBE growth technique can produce a nearly atomically clean surface in the growth procedure. Moreover in comparison to other epitaxial growth techniques, MBE has many advantages; (i) MBE has more precise control of the beam fluxes because of its UHV deposition technique, computer-controlled system and *in situ* surface sensitive diagnostic methods, (ii) MBE growth is governed mainly by the kinetics of the surface processes so it has more precise control of the growth condition. Because of these

powerful capabilities, MBE is enable the fabrication of sophisticated device structures (Franchi et al. 2003).

3.1.1 Solid-Source Molecular Beam Epitaxy System Overview

In this work, all samples were grown in a RIBER 32P solid-source molecular beam epitaxy (SS-MBE) machine. This III-V MBE system consists of four chambers (load-lock chamber, sample preparation or introduction chamber, transfer chamber and growth chamber) as shown in figure 3.1. The load-lock chamber is the first pre-vacuum stage to load substrates into the MBE system and also re-load the grown sample out. The next stage is introduction chamber that has heater for heat treatment process (preheat) of the substrate to outgas contaminations and moisture. The preheat process is done at 450 °C for 1 hour by substrate heating up and cooling down through computerized temperature-controller. The next chamber is transfer chamber that used to store fresh substrates before loading into growth chamber. Each chamber is obtained UHV condition ($\sim 10^{-10}$ Torr) by pumping system of an ion pump and a titanium (Ti)-sublimation pump. All chambers are separated by isolated gate valve. The samples are transferred from one chamber to each other by using a magnetic arm and cassette. Figure 3.2 shows a schematic drawing of RIBER 32P MBE growth chamber that is the heart of MBE system. The growth chamber is cooled by liquid nitrogen (LN_2) during growth to collect contaminations outgasing from the heating parts and produce more UHV pressure. The group-III and group-V elements are installed in high purity crucibles in separated Knudsen (K)-effusion cells (In, Ga and arsenic (As_4) are contained in Pyrolytic boron nitride (PBN) crucibles and phosphorus (P_2), GaP decomposition source, is contained in PBN crucible with Ga-trapping cap) and sublimated or evaporated by heaters. The cell temperatures are controlled by feedback from standard thermocouples (Tungsten-Rhenium, W-Re with 5% or 26% Re) through a computer. To acquire the real time information of growth process and chamber conditions during growth, *in situ* reflection high-energy electron diffraction is used for monitoring the growth of the crystal layers and quadrapole mass spectrometer is used for classifying the type and quantity of each molecule in chamber. A computer controls the beam flux by controlling molybdenum (Mo) main shutter and Mo shutter in front of each K-effusion cell, allowing precise control of layer composition, doping and thickness (down to a single layer of atoms).

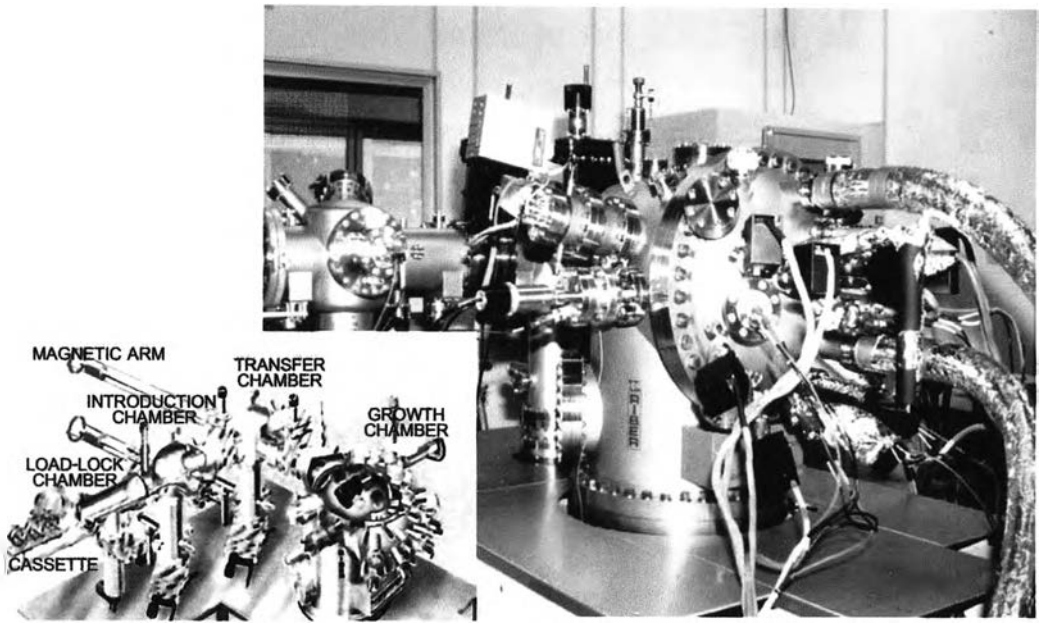

Figure 3.1 The RIBER 32P SS-MBE machine at semiconductor devices research laboratory (SDRL), Chulalongkorn University.

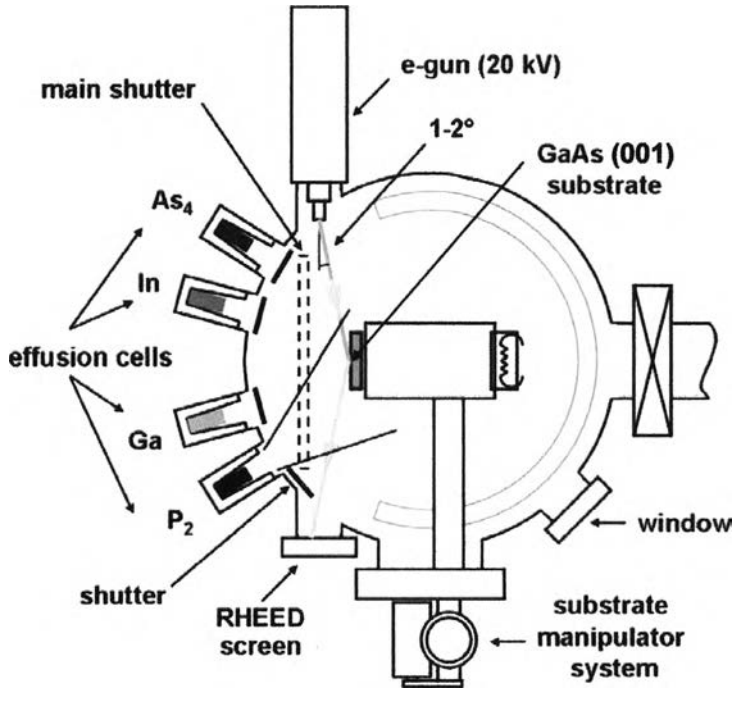

Figure 3.2 A schematic drawing of the RIBER 32P SS-MBE growth chamber.

3.2 Reflection High Energy Electron Diffraction

Reflection high-energy electron diffraction (RHEED) is an essential technique for surface structural and morphology analysis. It is remarkably simple to implement which an electron gun (10 to 20 keV), a RHEED (phosphor) screen, a charge-coupled device (CCD) camera, a computer and a clean surface are required. Figure 3.3 shows a schematic of the RHEED observation system. After a high-energy electron incident beam directed at a low angle (1-2°) to the sample surface, it is diffracted from elastically scattered atoms and reconstructs diffraction pattern appearing on the RHEED screen. Then the RHEED pattern is captured with a CCD camera and is displayed with the data processing software through the computer. RHEED is primarily sensitive to the atomic structure of first few planes of a crystal lattice owing to its small penetration depth that is the characteristic of the electron de Broglie wavelength. The diffraction beams interfere constructively and create pattern as shown in figure 3.4 (a). The pattern position can be graphically determined by the Laue method-intersection of Ewald sphere in reciprocal lattice space (Kittel, 1996). Therefore the surface configuration in the order of an atomic scale is represented by RHEED pattern perpendicular to the real surface. The condition for imaging on the RHEED screen is called the Laue diffraction condition:

$$\boldsymbol{k}_{\text{diff}} - \boldsymbol{k}_{\text{in}} = \boldsymbol{G} \tag{3.1}$$

where $\boldsymbol{k}_{\text{in}}$ and $\boldsymbol{k}_{\text{diff}}$ are the incident and diffracted electrons wave vectors, respectively, and $\boldsymbol{G}$ is the reciprocal lattice vector as shown in figure 3.4 (b). This condition corresponds to Bragg's law in the simple diffraction theory. If the surface has roughness, the surface layer in the reciprocal lattice space will be represented by a three-dimensional point array that is called spotty pattern. Figure 3.4 (c) shows an example of Ewald sphere construction for a reconstructed surface in $[1\,\bar{1}0]$ azimuth and RHEED pattern of GaAs (001) 2×4 surface in $[1\,\bar{1}0]$ and [110] azimuth that are called streaky patterns. The elongated streaks indicate the flat and smooth surface or a two-dimensional array and the broadening of the streaks indicates small area of coherence on the surface (Esser, 2001; Ichimiya and Cohen, 2004; LaBella, 1999).

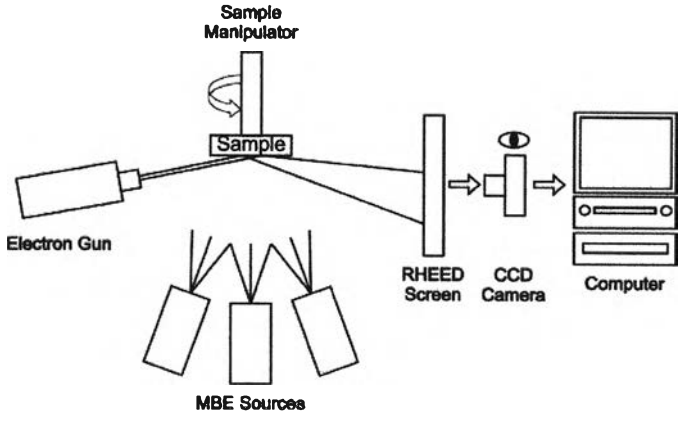

Figure 3.3 A schematic representation of the RHEED observation system.

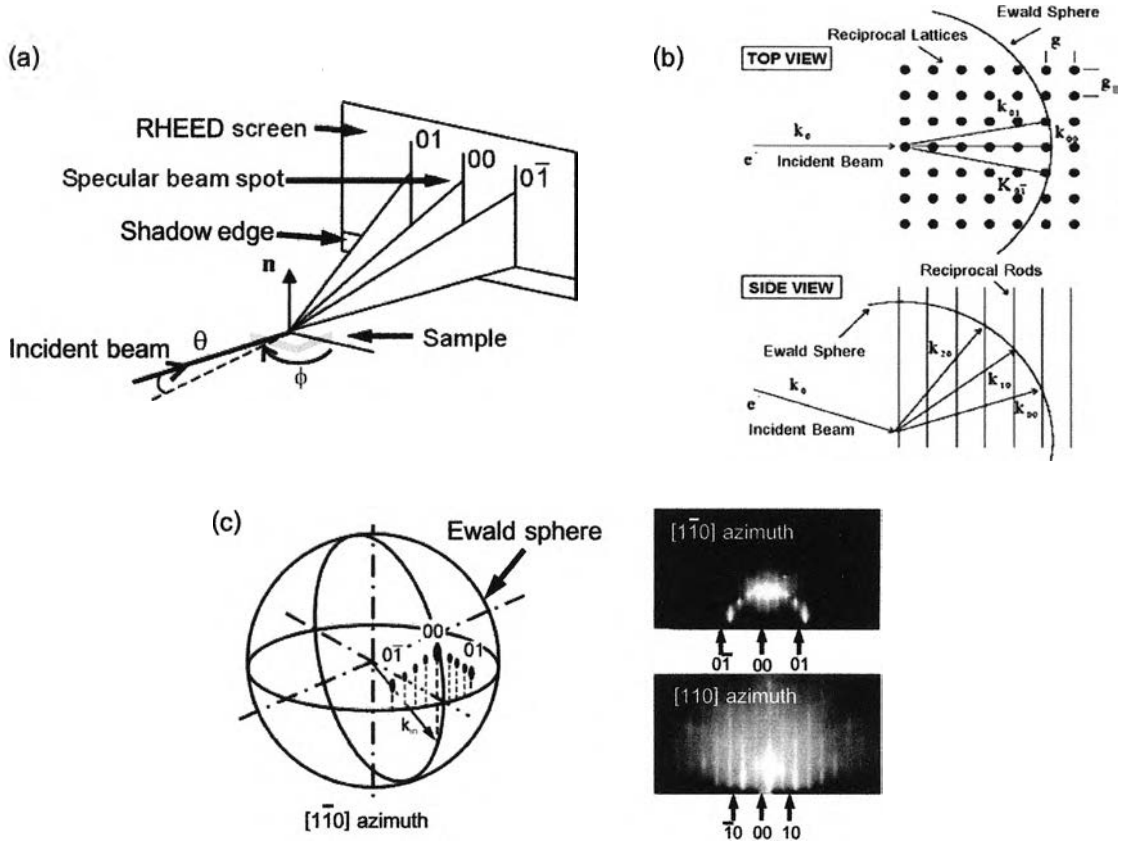

Figure 3.4 (a) a schematic representation of the RHEED geometry (Herman and Sitter, 1989), (b) the imaging of RHEED pattern that is determined by the Laue method-intersection of Ewald sphere in reciprocal lattice space and (c) an example of Ewald sphere construction for a reconstructed surface in [1 $\bar{1}$0] azimuth and RHEED pattern of GaAs (001) 2×4 surface in [1 $\bar{1}$0] and [110] azimuth (Ichimiya and Cohen, 2004).

3.2.1 RHEED Pattern Observation and Calibration

In general, the RHEED pattern provides information about a surface (Vvedensky, 2001) such as the crystallographic symmetry (from the symmetry of the diffraction pattern) and the extent of long-range order (from the sharpness of the pattern). In this work, RHEED observation are mainly used to indicates the self-assembled quantum dot (QD) formation by observing the pattern transition from streaky pattern (2 dimensions, 2D) to spotty pattern (3D) and deduce the absolute values of GaAs growth rate, GaP growth rate (equivalent to GaAs), InP growth rate (equivalent to InAs) and $In_xGa_{1-x}P$ alloy composition and growth rate (equivalent to $In_xGa_{1-x}As$) by observing the RHEED pattern transition and intensity oscillation to calculate the growth rate as a function of cell flux intensities or beam equivalent pressures (BEP). This RHEED observation is not only give the direct information of surface morphology and quality but also give indirect information such as substrate temperature and kinetics process of MBE growth. The transition of the reconstruction pattern as a function of substrate temperature is suitable to calibrate the absolute temperature of the substrate surface (Franke et al., 1998). In the specific case of the GaAs (001) surface, we can use the transition point from $c(4\times4)$ to (2×4) as a reference point. The details of the atomic configuration and the observed RHEED patterns of both the $c(4\times4)$ and the (2×4) reconstruction are shown in figure 3.5. In this work, this transition temperature is defined as 500 °C (Farrell and Palmstrøm, 1990). The RHEED pattern transition of temperature calibration process of GaAs in $[1\,\bar{1}0]$ azimuth is shown in figure 3.6. The RHEED pattern is changed by ramping the substrate temperature down and up from buffer growth temperature ($T_{buffer\ growth}$) at a rate of 10 °C/min under As-rich atmosphere. The transition temperature ($T_{transition}$) can be determined from average temperature of T_1, T_2, T_3 and T_4 is defined as 500 °C.

RHEED intensity oscillations can be used to extract the growth rate of GaAs and GaP (equivalent to GaAs). The schematic representation of the interpretation of RHEED intensity oscillation is shown in figure 3.7 (a). The RHEED intensity signal at every point on the pattern depends on the roughness of the surface. Under the normal growth condition, the RHEED intensity, i.e., surface roughness, changes according to the fraction of surface coverage where the period of the oscillation signal corresponds to the growth of 1 monolayer (ML). After starting growth of GaAs (coverage (δ) = 0 ML), 2D layer-by-

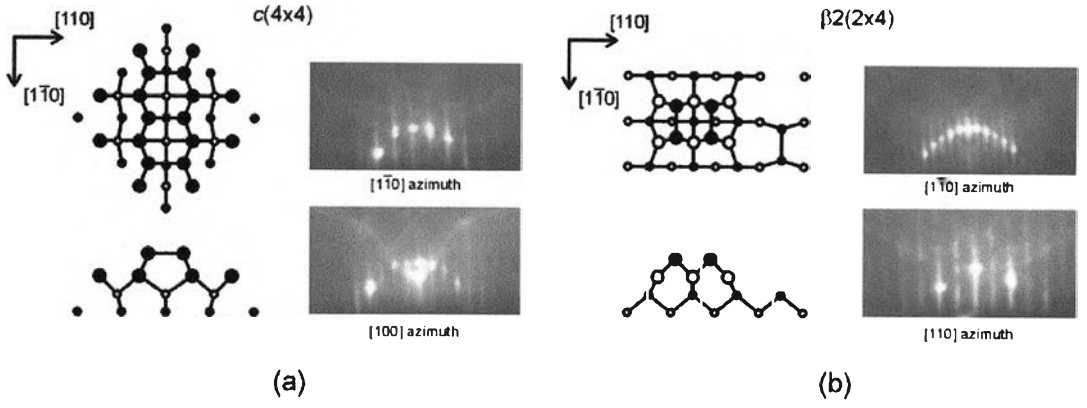

Figure 3.5 (a) Schematic representation of top view, side view of relaxed structure (Esser et al., 2001) and $c(4\times4)$ RHEED pattern of GaAs surface at 460°C in [1 $\bar{1}$0] and [100] azimuths; and (b) Schematic representation of top view, side view of relaxed structure (LaBella et al., 1999) and (2×4) RHEED pattern of GaAs surface at 580°C in [1 $\bar{1}$0] and [110] azimuths. Filled and empty circles represent As and Ga, respectively. Larger circles represent atoms closer to the surface.

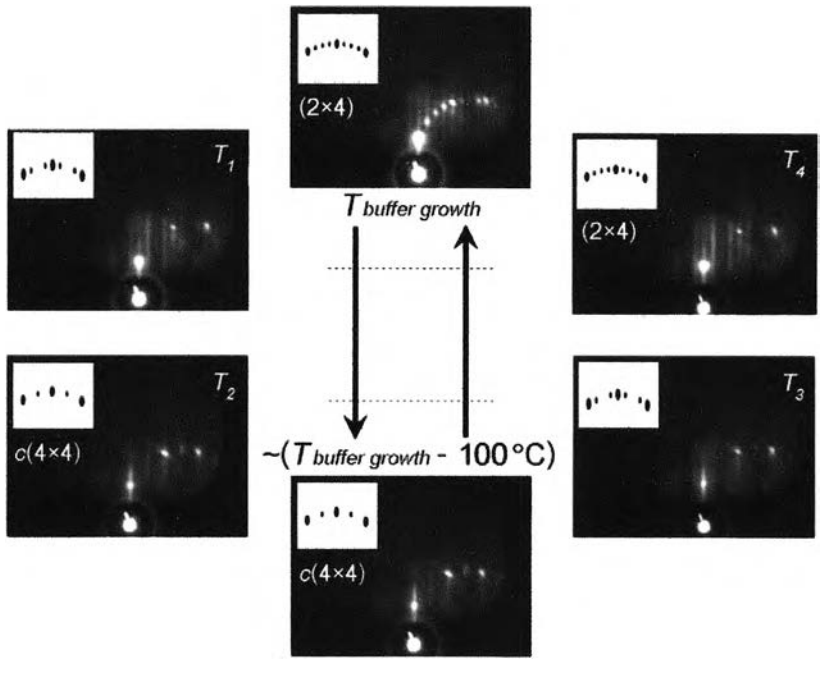

Figure 3.6 The RHEED pattern transition of temperature calibration process of GaAs in [1 $\bar{1}$0] azimuth ($T_{transition}$ (500 °C) = (T_1+T_2+T_3+T_4) / 4).

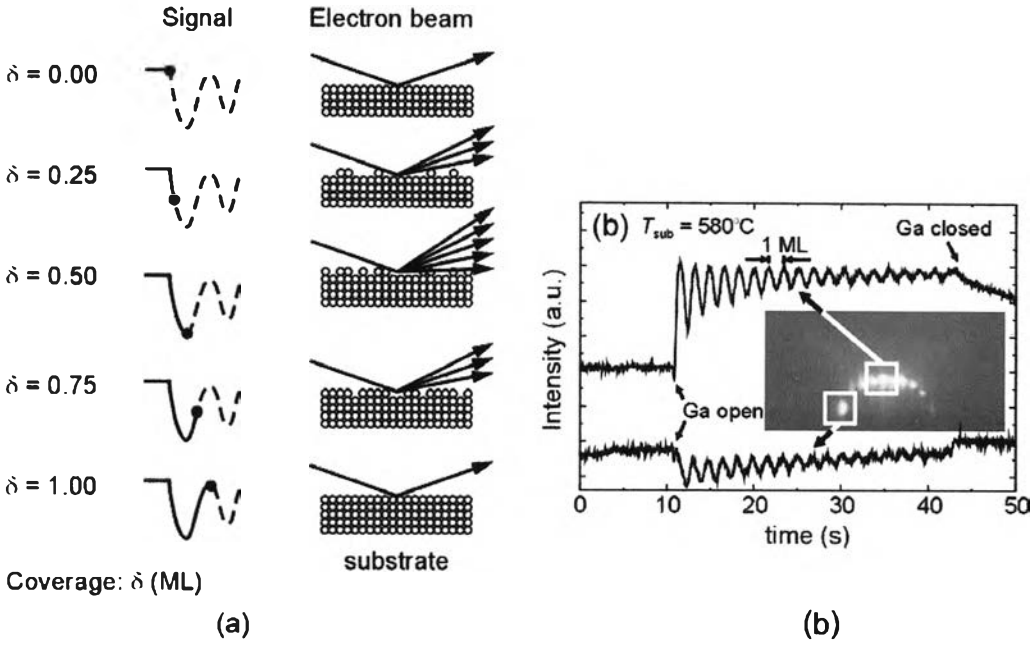

Figure 3.7 (a) Schematic representation of the interpretation of RHEED intensity oscillations and (b) are experimental results obtained during the growth of GaAs. The intensity signals were detected in the pattern area marked by white boxes shown in the insets (Shchukin and Bimberg, 1999).

layer islands or surface step features on the growing surface increase until they reach maximum value (δ = 0.5 ML). Due to higher surface density of steps, the diffracted beam intensity oscillation show a minimum of this growth stage. As the growth proceeds, 2D islands tend to coalescence and the density of atomic surface steps reduces (δ = 0.75 ML). Correspondingly, the diffracted beam intensity oscillation increases more. Finally, it reaches a maximum value when the GaAs coverage is 1 ML. The typical experimental data are shown in figure 3.7 (b). By this fact, the growth rate of GaAs can be calibrated. GaAs buffer layers are grown until *c*(2×4) RHEED reconstruction pattern is clearly seen. Then, Ga shutter is closed and the motor is stopped ay the position where the specular beam can be clearly seen. A stop watch is use to count the number of RHEED intensity oscillations starting with the highest intensity oscillation, typically 5 oscillations (δ = 4 ML). The growth rate is calculated by dividing the number of ML grown by the time. This process is repeated at different Ga temperatures. The growth rates of GaAs as a function of Ga BEP, calculated from the RHEED intensity oscillation experiment, are shown in figure 3.8 (a).

In case of the InAs and InP (equivalent to InAs), we use a different technique to calibrate the growth rate by using the QD formation time itself as the InAs growth rate calibration. The RHEED pattern transition during the growth of InAs which corresponds to the growth mode changeover from streaky (2D) to spotty (3D) pattern is defined as 1.7 ML InAs deposition (Shchukin and Bimberg, 1999). InAs QDs is grown on GaAs buffer layer at substrate temperature of 500 °C. The growth rate of InAs is defined ratio of 1.7 ML to the time taken from the opening of In shutter to when the 2D to 3D pattern transition occurs. InAs QDs is grown at different In BEP. The growth rate of InAs calculated from the RHEED pattern transition from 2D to 3D is shown in figure 3.8 (b). Note that all experiments are calibrated under constant As_4 BEP of 7×10^{-6} Torr. The relationship between the growth rate (in log scale) and the BEP was linearized in order to interpolate and extrapolate to the desired values.

The growth rate of InGaAs can also be determined from RHEED intensity oscillation by adding Ga during the InAs deposition with each fix InAs growth rate or by simply adding the growth rates of InAs and GaAs. The growth rates of InGaAs (r_{InGaAs}) can be written as

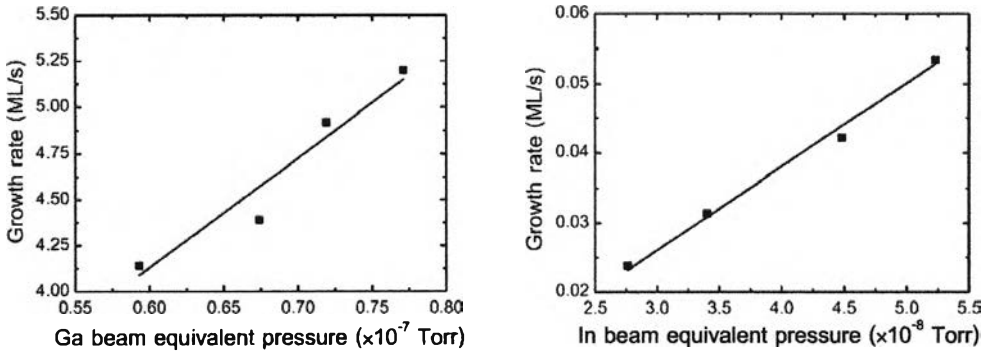

Figure 3.8 Plots of growth rates of GaAs (a) and InAs (b) as a function of cell BEP. The GaAs growth rates were calibrated by RHEED intensity oscillation while the InAs growth rate was obtained from RHEED pattern transition during the growth of self-assembled QDs. All RHEED data were obtained from a 2×2 cm^2 GaAs substrate glued in the middle of a molybdenum block under As-rich condition.

$$r_{InGaAs} = r_{InAs} + r_{GaAs} \tag{3.2}$$

where r_{InAs} and r_{GaAs} is the growth rates of InAs and GaAs, respectively. The alloy compositions of $In_xGa_{1-x}As$ and $In_xGa_{1-x}P$ (equivalent to $In_xGa_{1-x}As$) can simply determine by the relative group III fluxes reaching the surface since the sticking coefficients of group III elements are unity. The In composition (x_{In}) in $In_xGa_{1-x}As$ can be determined from

$$x_{In} = \frac{r_{InAs}}{r_{InAs} + r_{GaAs}} \tag{3.3}$$

From the alloy composition of $In_xGa_{1-x}P$ (equivalent to $In_xGa_{1-x}As$) equation, we need the In composition around 0.5 that has the lattice-matching with GaAs and the $In_{0.5}Ga_{0.5}P$ growth rate of 0.5 ML/s. The cell BEP that we have to use can be found. To check the $In_{0.5}Ga_{0.5}P$ growth rate and composition again, the $In_{0.5}Ga_{0.5}P$ layer grown on GaAs substrate is measured by scanning electron microscorpy (SEM), high resolution x-ray diffractometer (HRXRD) and photoluminescence (PL) measurement, respectively. The detailed experiments on SEM and HRXRD measurements of $In_{0.5}Ga_{0.5}P$ layer will be given in chapter 4.

3.3 Scanning Electron Microscopy

The scanning electron microscopy (SEM) is one of imaging techniques of electron microscopy. The sample surface is imaged by scanning it with a high-energy beam of electrons in a raster scan pattern. The electrons interact with the atoms making up the sample producing signals that contain information about the sample's surface topography, composition and other properties such as electrical conductivity, and then fed into an observation cathode ray tube (CRT). On the CRT, the information is used to control the brightness of the corresponding spot. The spot on the CRT is shown in real time with the electron beam scanning in the specimen surface. Thus, the information emitted from the specimen surface is displayed on the CRT as an image. The magnification of the displayed image is defined as the ratio of the size of the image on the CRT to size of the electron beam scanning on the specimen surface. In this work, the cross-sectional surface

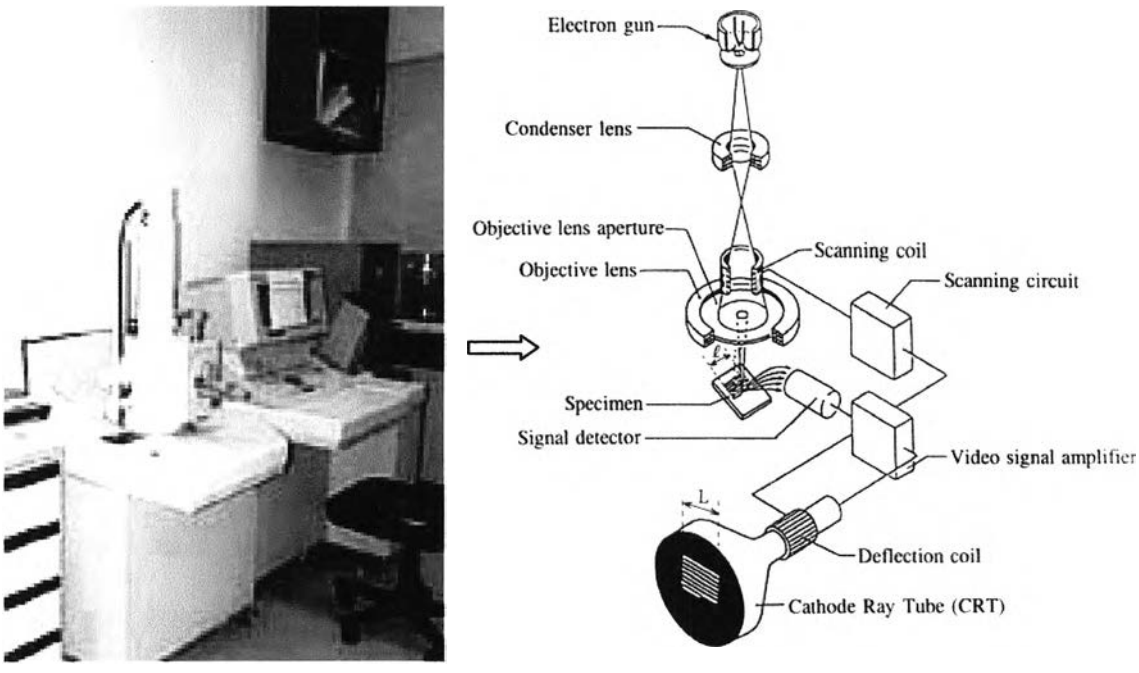

Figure 3.9 A JEOL JSM-5400 electron microscope at Analytical Instrument Center and Laboratory (AICL), Chulalongkorn University and schematic of SEM measurement.

of sample is desired to measure the thickness of InGaP layer. Prior to loading the sample into the chamber, the sample surface is coated with gold and the sample is set on the stage with the carbon tape to eradicate static surface charge for clear observation of each layer contrast. A JEOL JSM-5400 electron microscope that use in this work and schematic of SEM measurement are shown in figure 3.9. It has magnification from 15x to 200,000x and can be operated between 0.5 to 30 kV with point resolution of 4 nm.

3.4 High Resolution X-Ray Diffractometer

High resolution X-ray diffractometer (HRXRD) is a powerful and commonly available technique for identifying the presence of crystalline phase. The quantitative, high-accuracy measurements of interatomic spacing provided by HRXRD have motivated some detailed studies. The XRD patterns also provide information on strain and preferential orientation of epitaxial layer. In addition, HRXRD is non-destructive and can sometimes be used *in situ*. X-rays with wavelength, λ, between 0.5 Å and 2 Å are

impinged upon a sample. The diffracted x-rays are measured at 2θ, the angle between x-ray source and detector. Diffracted waves from different atoms can interfere with each other and the resultant intensity distribution is strongly modulated by this interaction. If the atoms are arranged in a periodic fashion, as in crystals, the diffracted waves will consist of sharp interference maxima (peaks) with the same symmetry as in the distribution of atoms. Measuring the diffraction pattern therefore allows us to deduce the distribution of atoms in a material. The peaks in an x-ray diffraction pattern are directly related to the atomic distances. Let us consider an incident x-ray beam interacting with the atoms arranged in a periodic manner as shown in 2 dimensions in figure 3.10. The atoms, represented as green spheres in the graph, can be viewed as forming different sets of planes in the crystal (colored lines in graph on left). For a given set of lattice planes with an inter-plane distance of *d*, the condition for a diffraction (peak) to occur can be simply written as

$$2\,d \sin\theta = n\,\lambda \tag{3.4}$$

which is known as the Bragg's law. The Bragg's Law is one of most important laws used for interpreting x-ray diffraction data. In the equation, λ is the wavelength of the x-ray, θ is the scattering angle, and *n* is an integer representing the order of the diffraction peak. In this work, The XRD patterns of InGaP layer grown on GaAs substrate are performed by using PHILIPS X' Pert PRO diffractometer. The In composition is calibrated to grow the InGaP layer which has lattice-match with GaAs. The HRXRD machine is shown in figure 3.11.

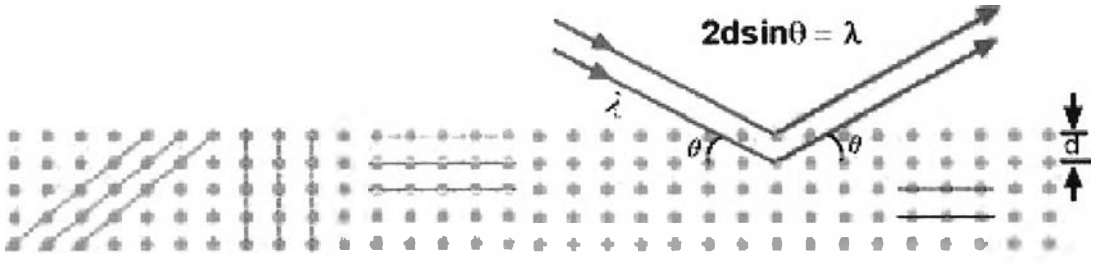

Figure 3.10 Lattice planes and Bragg's law.

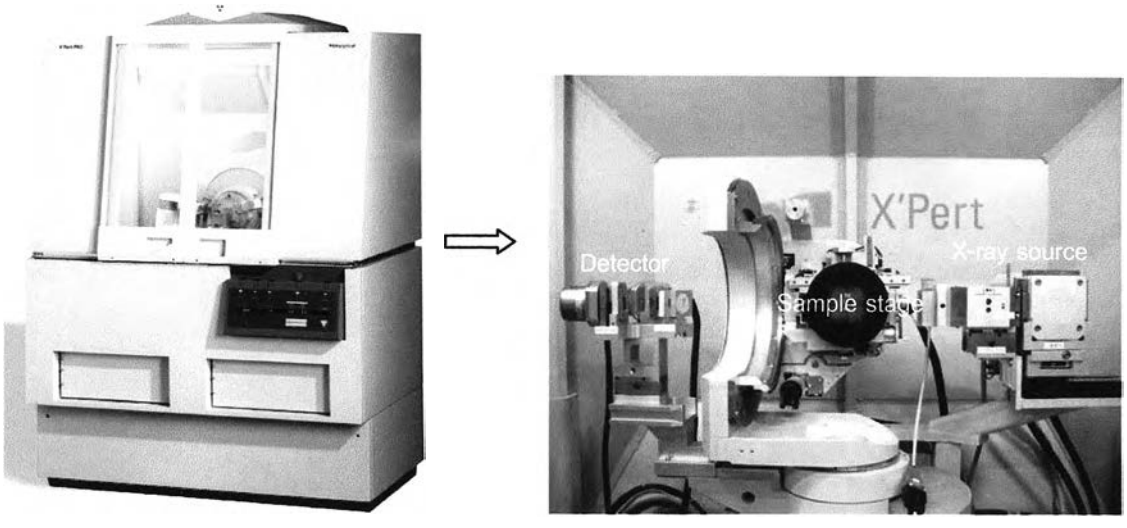

Figure 3.11 The PHILIPS X' Pert PRO diffractometer at Nakano-Sugiyama-Tanemura Laboratory,The University of Tokyo.

3.5 Atomic Force Microscopy

The atomic force microscopy (AFM) is a very high-resolution type of scanning probe microscope, with demonstrated resolution of fractions of a nanometer. The AFM consists of a microscale cantilever with a sharp tip (probe) at its end that is used to scan the surface, photodiodes and feedback electronics. The cantilever is typically silicon or silicon nitride with a tip radius of curvature in the order of nanometers. When the tip is brought into proximity of a sample surface, the van der Waals forces between the tip and the sample lead to a deflection of the cantilever. Typically, the deflection is measured using a laser spot reflected from the top of the cantilever into an array of photodiodes. The sample is mounted on a piezoelectric tube, which can move the sample in the z direction for maintaining a constant force, and the x and y directions for scanning the sample. The feedback mechanism is responsible for adjusting the tip-to-sample distance in order to avoid the physical contact between them during scanning. In this work, the AFM images are performed by using SEIKO SPA 400-AFM. The SEIKO SPA 400-AFM and a schematic of AFM measurement are shown in figure 3.12 and modes of AFM measurement are shown in figure 3.13.

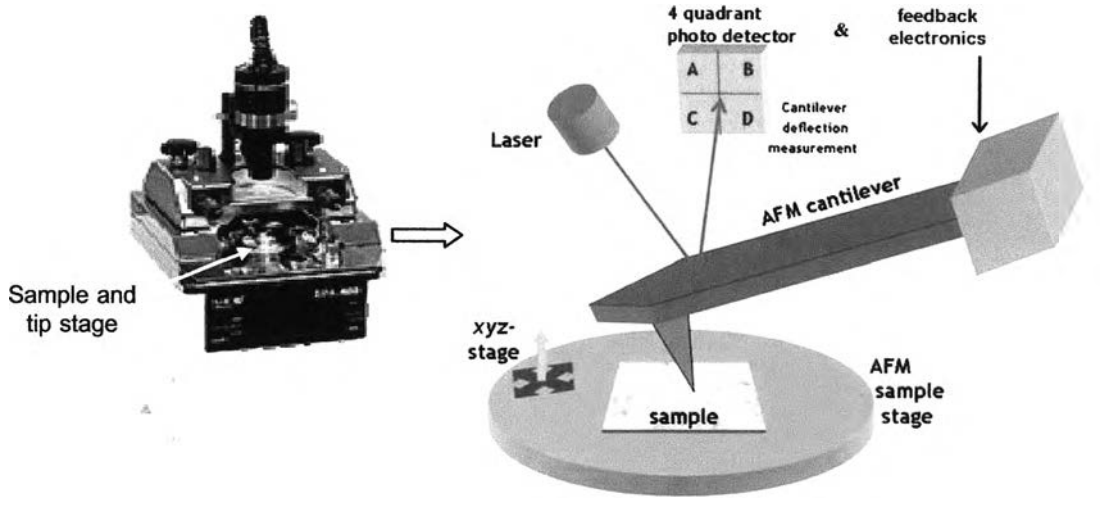

Figure 3.12 The SEIKO SPA 400-AFM at SDRL, Chulalongkorn University and a schematic of AFM measurement.

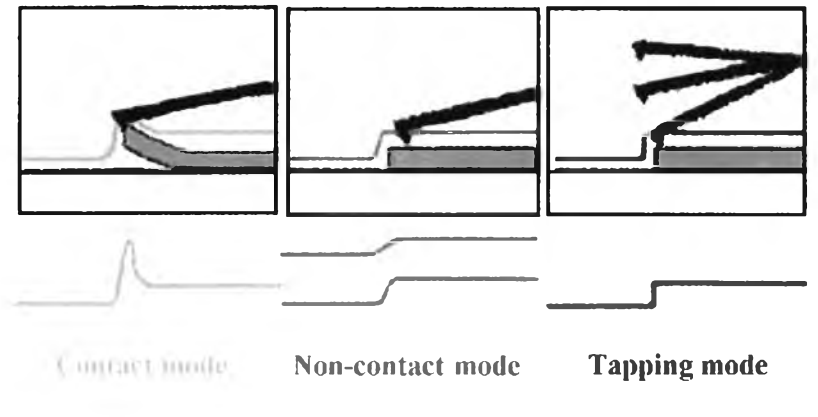

Figure 3.13 Modes of AFM measurement.

The AFM can operate in three modes: contact mode, non-contact mode and dynamic contact mode or tapping mode. In the contact mode operation, a constant deflection is maintained to keep the force constant during the scaning, In the non-contact mode, the cantilever is osillated externally in order to avoid tip-sample contact. In tapping mode, the cantilever is oscillated so that the tip come into contact with the sample in each pediod of scanning. Freguency and amplitude modulations provide surface information in the non-contact and tapping modes. The change in osillation freguency provides quantitative

information of the sample while the change in amplitude provides topographic information of the sample.

In this work, the AFM is operated in the tapping mode. The scan rate is around 1-2 Hz corresponding to the scan area that is usually 5×5 μm^2, 2×2 μm^2, 1×1 μm^2 and 0.5×0.5 μm^2. If the scan size is big, the scan rate will be high. The number of data points per scan line is 512. Due to the tip convolution (Keller and Franke, 1993; Gong et al., 1998), the exact shape and lateral size of the QD structure may not be correctly determined by this measurement. Nevertheless, the resolution of this measurement is usually in subnanometer range. In this work, we use the analysis of the AFM images to determine the densities of InP QDs, InP ring-shaped quantum dot molecules (QDMs), outer and inner diameters of InP ring-shaped QDMs and the distributions of the number of InP QDs per InP ring-shaped QDMs, lateral size distribution and height distribution of InP QDs.

3.6 Transmission Electron Microscopy

Transmission electron microscopy (TEM) is another one of imaging techniques of electron microscopy. The sample must be polish until thin enough to allow electrons to transmit through. In the measurement, emitted electron beams from the source are incident on the sample, diffracted by the atoms and then transmitted to the other side of the sample and are focused by an objective lens and amplified by magnifying or projector lens. After that the amplified electron beams hit a florescence screen and the information about the inner structure of the sample is displayed in real time on the monitor. By using selected area electron diffraction aperture located between the objective and projector lenses, bright- and dark-field images can be selected. In the bright-field image, the aperture only allows, undeviated electrons to pass through and form image at the screen. On the other hand, only one of beams reflected from a particular plane is allowed by the aperture in the dark-flied image. Dark-field imaging thus depends on the particular diffracted beam selected. A JEOL JEM-2010 electron microscope that use in this work and its schematic diagram are shown in figure 3.14. It has a Lanthanum Hexaboride (LaB_6) electron gun and can be operated between 80 to 200 kV with point resolution of 0.23 nm.

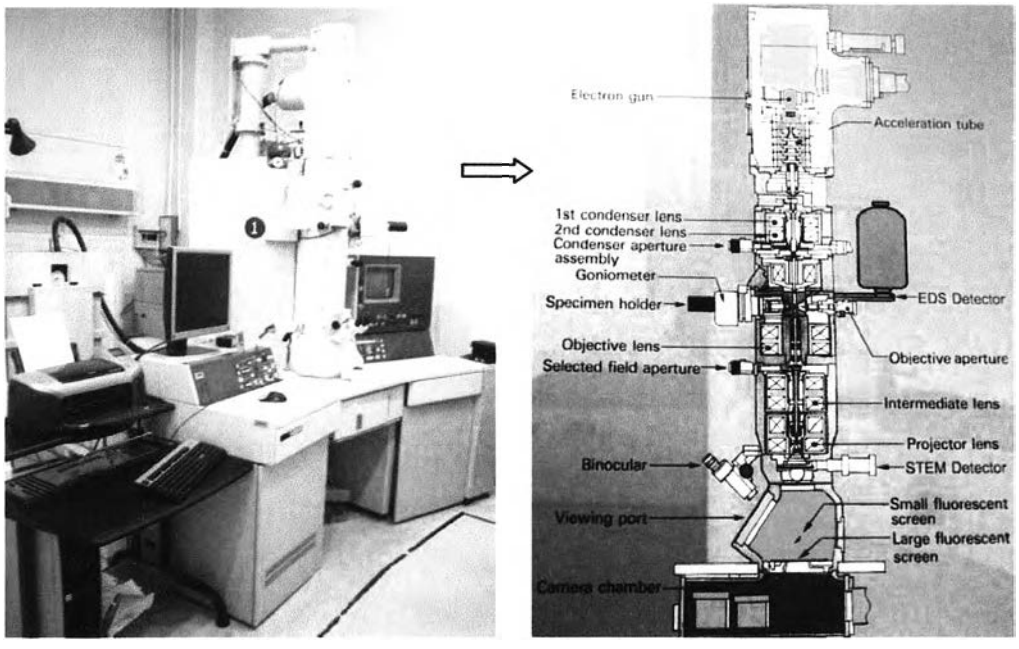

Figure 3.14 A JEOL JEM-2010 electron microscope at National Electronics and Computer Technology Center (NECTEC) and its schematic diagram.

3.7 Photoluminescence Spectroscopy

The main tool for the optical characterization of sample is the photoluminescence (PL) spectroscopy. In this work, the samples which are buried self-assembled InP ring-shaped QDMs in $In_{0.5}Ga_{0.5}P$ is measured by two PL systems. The first system is micro-PL and the second one is macro-PL. The micro-PL system is shown in figure 3.15. The samples are excited by a diode-pumped solid state laser (DPSS-VANTUS 532). The laser emits light in green region of spectrum at 532 nm with laser spot size 1-2 μm and is a laser system for powers in excess of 500 mW. The laser beam was chopped and focused to the sample. The light signal is resolved by a monochromator. The filter is used to filter the reflected laser beam signal. The resolved light signal is detected by a LN_2-cooled CCD detector at room temperature. This system has a high power laser but it can measure only at room temperature (RT) or 300 K. Therefore, the macro-PL is used to study the temperature dependent of InP ring-shaped QDMs.

For the second system, a schematic of the macro-PL experimental setup is shown in figure 3.16. The samples are excited by the 478-nm line of an Ar^+ laser (SPECTRA

PHYSICS SERIES 2000). The laser emits light in blue region and its power can vary from 10 mW to 80 mW for measuring PL spectra. The sample temperature can vary from 20 K to RT. The laser beam was chopped and focused to the sample by a 33-cm focal length lens. An 8-cm focal length and a 40-cm focal length lens are used to collect the PL signal. The light signal is resolved by a 1-m monochromator (JOBIN YVON THR1000). The entrance and exit slit widths are 3 mm. The resolved light signal is detected by a LN_2-cooled InGaAs detector (HAMAMATSU G7754-01 with 0.1-mm^2 active area). A chopper, the lock-in amplifier (EG&G 5207) and digital multimeter are used to enhance the signal by the standard lock-in technique. For low-temperature and temperature dependent measurements, the sample was mounted on the cold finger of a closed-cycle cryostat.

In this work, the interpretation of PL data can simply be described as shown in figure 3.17 and figure 3.18. For a case of QDs with different size in figure 3.17, the ground state PL peak energy contains information about the size of the QD. The increase in QD size results in a lower quantized energy levels of both holes and electrons, which causes a lower PL peak energy position. Therefore, this PL peak position can be used to relatively compare the size of QD structure.

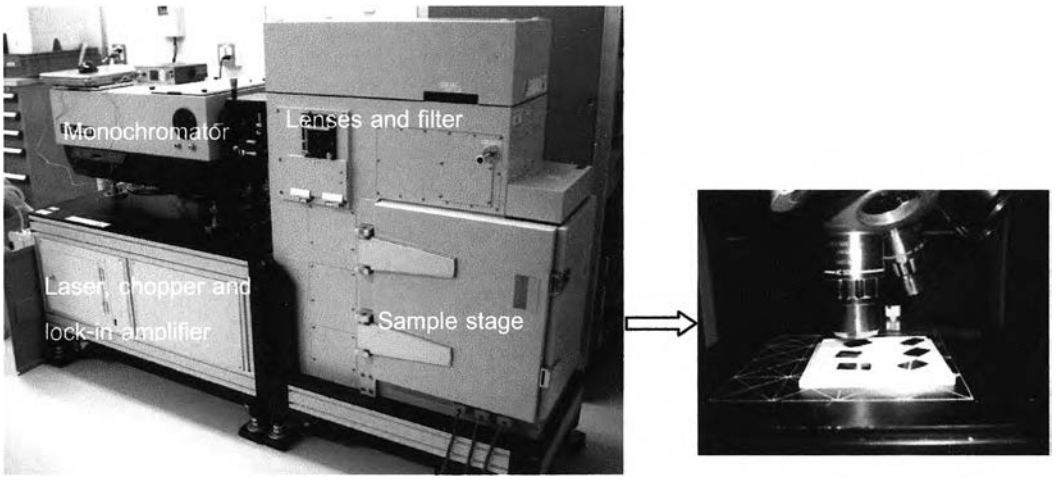

Figure 3.15 The micro-PL system at Nakano-Sugiyama-Tanemura Laboratory, The University of Tokyo.

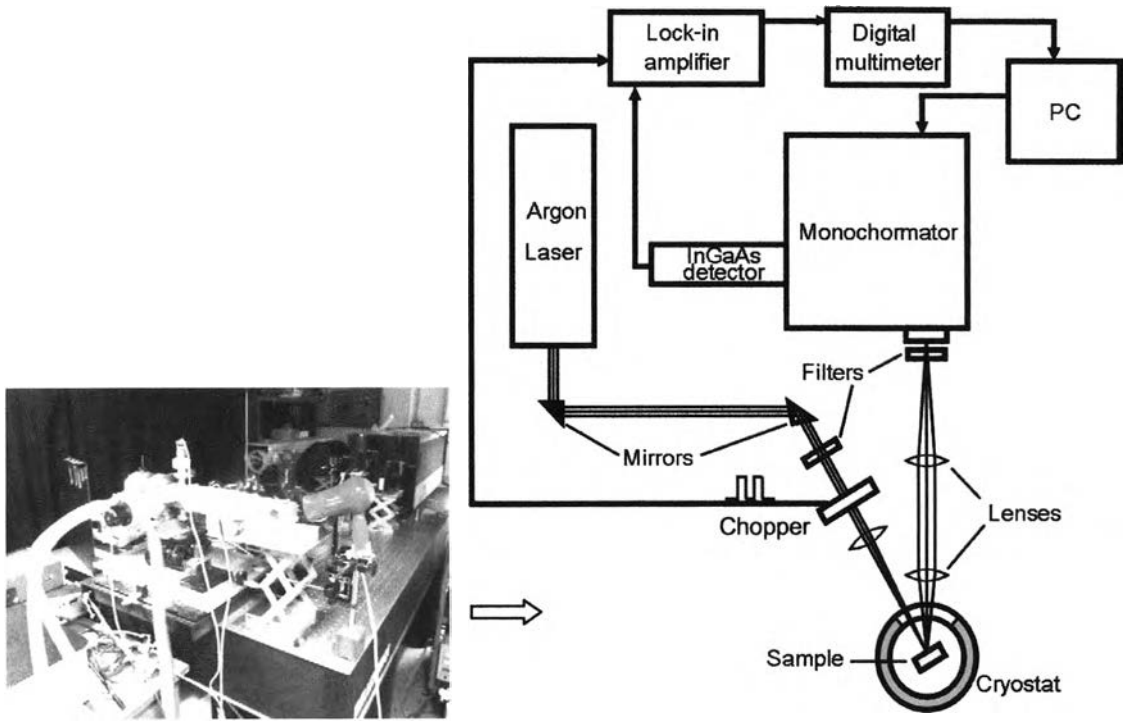

Figure 3.16 The macro-PL setup and its schematic at SDRL, Chulalongkorn University.

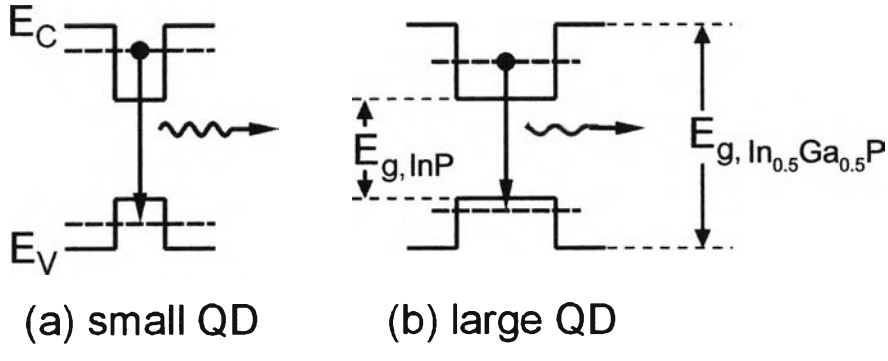

Figure 3.17 Simple interpretation of the PL data obtained from a QD structure. In case of small QD (a): the PL peak energy position is higher compared with large QD (b).

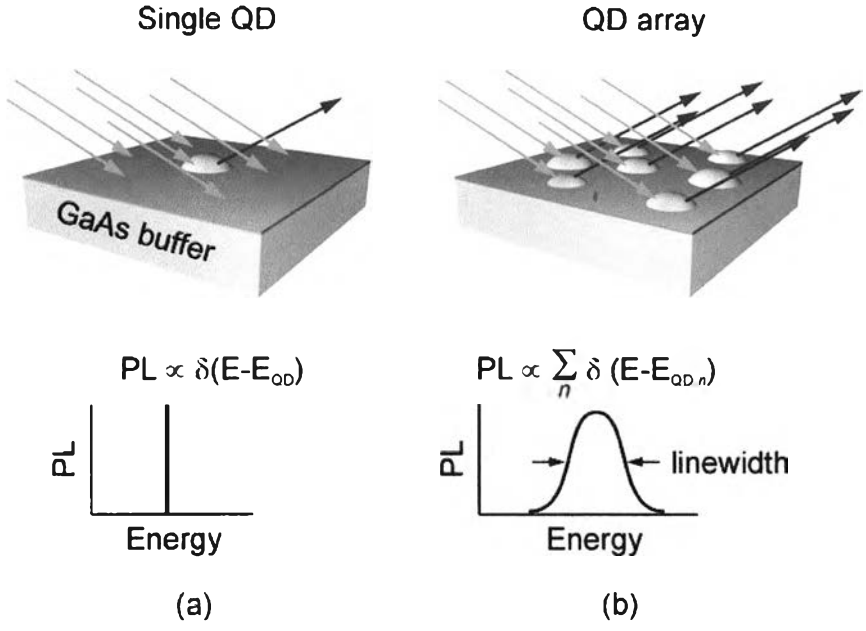

Figure 3.18 Simple interpretation of the PL spectrum obtained from the QD structure. In (a) the PL spectrum is very narrow due to the delta-function like density of states; and in (b) the average dot size corresponds to the PL peak energy position and the PL linewidth corresponds to the size distribution of the array.

For the shape of PL spectrum from QD array in figure 3.18, there exists broadening there exists broadening of the spectrum. This broadening, which is measured in terms of a full width at half (FWHM) or PL linewidth, is related to the QD size distribution. From experiments on single QD spectroscopy, we know that if the array contain a few number of QDs, the PL linewidth will usually less than 0.1 meV (Zrenner, 2000), which corresponds to the delta-function-like density of states. However, in case of self-assembled QDs, there are large numbers of excited QDs, which have different size. This difference in QD sizes results in rather broad PL spectrum (~ 10-100 meV). The PL spectroscopy is therefore very important as it can be used to determine the homogeneity of the QD. Another interpretation of PL results come from the fact that the loss of coherence and the onset of misfit dislocations in the epitaxial film create a high concentration of centers of nonradiative recombination and significantly reduce the integrated intensity of PL spectrum. Therefore, we can roughly estimate and compare the defect density in grown structure by comparing the PL intensity.

3.8 Sample preparation

The detailed steps for sample preparation are as follows. First, an approximately 2×2-cm^2 piece of epi-ready semi-insulating (001) GaAs wafer was glued onto a molybdenum block by using indium glue. After transferring of the wafer into the introduction chamber, the block with the wafer was heated in the introduction chamber 450°C for 1 hour in order to decontaminate the wafer from moisture (H_2O). Prior to main growth, surface oxide desorption was done under As_4 BEP of 6×10^{-6} Torr. The surface oxide was desorbed by slowly ramping substrate temperature to 610 °C and waiting for 15 minutes. At this stage, the RHEED pattern is carefully observed to find a deoxidation temperature when the RHEED pattern showed abrupt transformation from 2×4 surface reconstruction to roughness surface pattern of oxide desorption. After that, a 100-nm-thick GaAs buffer layer was first grown at a deoxidation temperature with a growth rate of 0.5 ML/s. During this process, the temperature calibration process is performed to obtain the actual surface temperature. And then, a 200-nm-thick GaAs buffer layer was further grown to smooth the sample surface. The sharp and clear 2×4 RHEED pattern (streaky pattern) is observed after finishing the growth of this buffer layer. Next, the environment inside the growth chamber was changed from As atmosphere to P atmosphere. These are followed by the growth of 200-nm-thick $In_{0.5}Ga_{0.5}P$ layer at substrate temperature of 470 °C with a BEP V/III ratio of 10 and growth rate of 0.5 ML/s. During the growth of $In_{0.5}Ga_{0.5}P$ layer, RHEED showed a 2×1 surface reconstruction. Then, the substrate temperature was reduced to 250 °C without P_2 beam to minimize the excess P on the surface. Before depositing the indium, we reduced the background pressure of the growth chamber to less than 10^{-9} Torr to minimize the initial interaction between indium and phosphorus during the indium deposition. To investigate the effect of deposition temperature, crystallization temperature, indium deposition rate and indium thickness, four sample series were fabricated. For the first series, different deposition temperatures of 120 °C, 150 °C, 180 °C, 210 °C, 250 °C, and 290 °C, were varied with same indium thickness of 3.2 ML, indium deposition rate of 0.8 ML/s and crystallization temperatures of 200 °C. For the second series, different crystallization temperatures of 150 °C, 200 °C, 250 °C and 300 °C were varied with same deposition temperature of 250 °C, indium thickness of 3.2 ML and indium deposition rate of 1.6 ML/s. For the third series, an indium amount of 3.2 ML was deposited at same deposition temperature of

250 °C and crystallization temperatures of 200 °C with different indium deposition rate of 0.2 ML/s, 0.4 ML/s, 0.8 ML/s and 1.6 ML/s respectively. For the fourth series, a different amount of indium, 1.6 ML, 3.2 ML, 4.8 ML and 6.4 ML, was deposited on $In_{0.5}Ga_{0.5}P$ layer with same indium deposition rate of 1.6 ML/s and same deposition temperature of 250 °C and crystallization temperatures of 200 °C. The crystallization processing was achieved under 4×10^{-6} Torr of P_2 BEP for 5 minutes. The surface morphologies were observed using a tapping mode AFM. In order to perform PL measurements, a 100-nm-thick $In_{0.5}Ga_{0.5}P$ capping layer was grown after crystallization using two-step growth. First, a 10-nm-thick $In_{0.5}Ga_{0.5}P$ was grown by migration enhanced epitaxy (MEE) technique at 300 °C with 0.5-ML/cycle growth rate. Then a 90-nm-thick $In_{0.5}Ga_{0.5}P$ was growth by conventional epitaxy growth (CE) at 470 °C with 0.5-ML/s growth rate. Finally, the repeatable growth of InP ring-shaped QDMs was done again on the top of sample for cross-sectional observation by TEM, respectively. Figure 3.19 shows a schematic diagram of sample structure grown in this work.

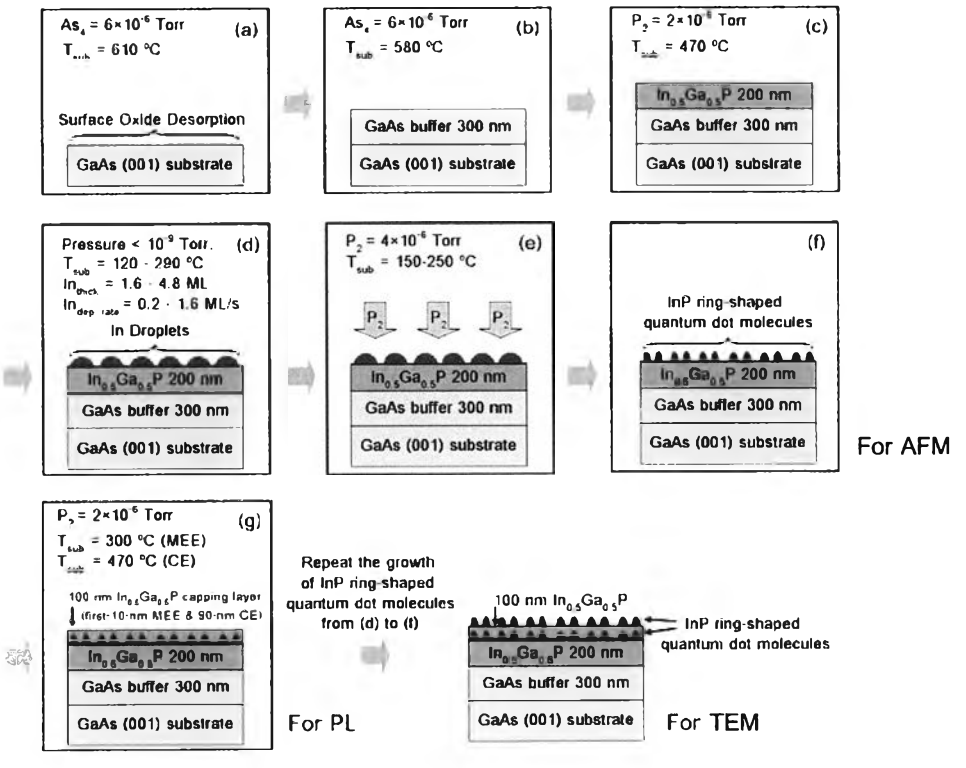

Figure 3.19 Schematic diagram of the sample structure grown in this work. The growth conditions for the InP ring-shaped QDMs layer were given in the text.